



Tantala Kerr nonlinear integrated photonics

HOJOONG JUNG,^{1,2,3} SU-PENG YU,^{1,2} DAVID R. CARLSON,¹  TARA E. DRAKE,¹
TRAVIS C. BRILES,^{1,2} AND SCOTT B. PAPP^{1,2,*} 

¹Time and Frequency Division, National Institute of Standards and Technology, 325 Broadway, Boulder, Colorado 80305, USA

²Department of Physics, University of Colorado, 390 UCB, Boulder, Colorado 80309, USA

³Current Address: Center for Quantum Information, Korea Institute of Science and Technology, Seoul, Republic of Korea

*Corresponding author: scott.papp@nist.gov

Received 7 October 2020; revised 3 April 2021; accepted 22 April 2021 (Doc. ID 411968); published 26 May 2021

Integrated photonics plays a central role in modern science and technology, enabling experiments from nonlinear science to quantum information, ultraprecise measurements and sensing, and advanced applications such as data communication and signal processing. Optical materials with favorable properties are essential for nanofabrication of integrated photonics devices. Here we describe a material for integrated nonlinear photonics, tantalum pentoxide (Ta_2O_5 , hereafter tantala), which offers low intrinsic material stress, low optical loss, and efficient access to Kerr nonlinear processes. We utilize >800 nm thick tantala films deposited via ion beam sputtering on oxidized silicon wafers. The tantala films contain a low residual tensile stress of 38 MPa, and they offer a Kerr index of $n_2 = 6.2 \pm 2.3 \times 10^{-19} \text{ m}^2/\text{W}$, which is approximately a factor of 3 higher than silicon nitride. We fabricate integrated nonlinear resonators and waveguides without the cracking challenges that are prevalent in stoichiometric silicon nitride. The tantala resonators feature an optical quality factor up to 3.8×10^6 , which enables us to generate ultrabroad bandwidth Kerr soliton frequency combs with low threshold power. Moreover, we characterize tantala waveguides by supercontinuum generation from low-energy, ultrafast seed pulses. These demonstrations characterize future application directions with tantala integrated nonlinear photonics.

<https://doi.org/10.1364/OPTICA.411968>

1. INTRODUCTION

Nonlinear interactions of light and material enable powerful controls for electromagnetic fields. Kerr processes in particular allow wavelength conversion of laser light from one frequency to another [1] and generation of patterns [2] and solitary excitations [3,4] that have many uses. Key use examples include Kerr-microresonator frequency combs based on dissipative solitons [4], which enable frequency-comb functionalities with integrated photonics [5,6], and efficient supercontinuum generation in photonic waveguides, which extends the capabilities of fiber-based mode-locked lasers [7]. Leveraging Kerr nonlinearity generally requires low losses that allow extended light-matter interaction, and realization of nearly arbitrary phase-matching conditions. Nanofabrication powerfully enables nonlinear processes by enhancing intensity with small mode volume and by precise lithographic pattern transfer and heterogeneous combinations of materials that facilitate nonlinear phase matching. These properties are also enabling for integrated (linear) photonics applications, including microwave photonics [8], high-speed optical communication [9], and heterogeneous electronic-photonic integration of lasers and other devices [10]. Therefore, ideal materials are versatile and robust, straightforwardly allowing heterogeneous integration.

Stoichiometric silicon nitride (Si_3N_4 , hereafter SiN) obtained via low-pressure chemical vapor deposition is an exemplary material for Kerr nonlinear photonics, offering exceptionally low optical

loss [11], moderately strong Kerr nonlinear coefficients [12], and compatibility with CMOS semiconductor nanofabrication [12]. Still, large, intrinsic tensile stress (>1 GPa) is a particular challenge with SiN that leads to formation of cracks in the photonics layer [4]. Crack-mitigation strategies require additional, specialized processing steps, including combinations of thermal cycling [13] and damascene growth [14]. Besides SiN, several other photonic integration materials have been used for the benchmark application of Kerr soliton generation, including silica with silicon nitride waveguides [15], deuterated silicon nitride [16], soliton crystals in Hydrex [17], aluminum nitride [18], (aluminum) gallium arsenide [19], lithium niobate [20], and gallium phosphide [21].

We demonstrate low-loss, integrated nonlinear photonics in a new platform—tantalum pentoxide (Ta_2O_5 , hereafter tantala)—which offers excellent material properties to leverage Kerr nonlinearity. Tantala is a dielectric, CMOS-compatible material that has been used in microelectronics [22]. Tantala deposited by ion-beam sputtering (IBS) has long been used in low-loss, high-reflectivity mirror coatings for various fundamental experiments [23]. Over the past four decades at least, tantala has attracted great attention as a photonic material due to its high refractive index, large bandgap, low stress, low optical loss, low thermo-optic coefficient, and factor of 3 higher nonlinearity than SiN [24,25]; the majority of tantala's properties [26–30] are comparable or superior to SiN. Recently, IBS-deposited tantala has been used for photonic waveguide fabrication [27] due to its high transparency.

In low-confinement tantala-core waveguides, an ultralow loss of 3 dB/m has been reported [27]. However, high-confinement resonators have only been explored with RF sputtered tantala, and only relatively low quality factor (Q) has been reported [24]. Four-wave mixing experiments with high-confinement tantala waveguides and relatively low optical loss (1.5 dB/cm) have been reported [24,31,32].

In this paper, we report on nanofabrication of high intrinsic $Q_{\text{int}} > 3.8 \times 10^6$ integrated ring resonators and high-confinement waveguides, using tantala photonics layers up to 820 nm thick. Moreover, we explore frequency-comb applications with tantala. The low tensile stress of tantala ensures fabrication of a crack-free photonics layer without the specialized processing required with SiN. We generate Kerr soliton frequency combs with tantala ring resonators, which offer a low parametric oscillation threshold power. Furthermore, we demonstrate supercontinuum generation spanning 1.6 octaves with tantala waveguides with as little as 60 pJ of coupled mode-locked laser energy at 1560 nm. We report various tantala material properties, including the n_2 and thermo-optic coefficients that we estimate are $6.2 \pm 2.3 \times 10^{-19} \text{ m}^2/\text{W}$ and $8.8 \times 10^{-6}/\text{K}$, respectively. Tantala is a versatile material, offering wide opportunities for heterogeneous integration of low-loss and nonlinear photonics due to low-temperature deposition and processing requirements.

2. EVALUATION OF TANTALA FOR INTEGRATED NONLINEAR PHOTONICS

Figure 1 explores our tantala material, nanofabrication procedure, and ring resonator characterization. We begin with a tantala film of either 570 nm or 820 nm thickness, which is deposited by way of IBS on a thermally oxidized Si wafer. Two thicknesses are chosen to satisfy two types of phase-matching conditions, one

for a top air-cladded waveguide (570 nm) and another for a top silica-cladded waveguide (820 nm). The tantala-IBS service is provided by FiveNine Optics, which offers tantala and SiO₂ Bragg reflectors with part-per-million losses [23]. IBS deposition is versatile, offering designable layer stacks of several micrometers, with high uniformity on large substrates. We characterize the material to understand the potential for high-yield, wafer-scale nanofabrication. First, as shown in Fig. 1(a), we couple a 633-nm laser (Metricon 2010/M prism coupler) to an unpatterned tantala-on-insulator film to visualize cracking and scattering, which has not been observed in the course of fabricating with dozens of wafers. This technique demonstrates a measurement-limited $<0.3 \text{ dB/cm}$ scattering and absorption loss. Second, as shown in Fig. 1(b), we characterize the tantala thickness and stress distributions across a wafer, using the prism coupler for thickness and a multibeam laser system for stress, respectively. Nine points [open circles in Fig. 1(b)] indicate a uniform film thickness. Typically, tantala films are compressively stressed [29], and our as-sputtered film also shows a compressive stress of 170–210 MPa. Thermal annealing to 600°C, which we also use to reduce optical losses (see below), results in a low tensile stress in the central portion of the wafer. The color map in Fig. 1(b) shows the measured stress profile with slightly higher values only at the edges due to the wafer fixture.

With tantala-on-insulator wafers, we fabricate integrated nonlinear photonics, such as ring resonators; see Fig. 1(c). A typical device is 46 μm in diameter, and the ring waveguide width (RW) is 1.5 μm . Our fabrication process [Fig. 1(d)] involves electron-beam lithography, using a JEOL JBX-6300 FS system and ZEP-520A resist, and pattern transfer, using fluorine (CF₄ + Ar) inductively coupled plasma reactive-ion etching (ICP RIE). Scanning electron microscope (SEM) images and ring resonator spectroscopy experiments indicate that our lithography pattern

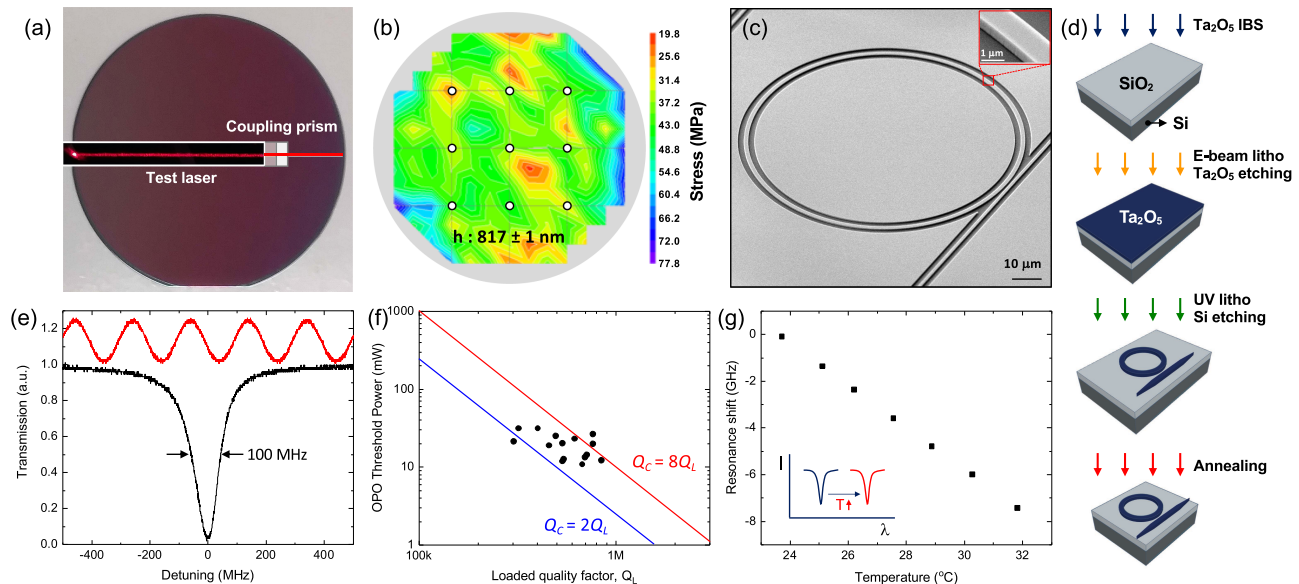


Fig. 1. Tantala material properties for integrated nonlinear photonics. (a) Photograph of a crack-free, 820 nm thick tantala layer on a thermally oxidized Si wafer. A laser is prism-coupled to the tantala layer and propagates across the entire wafer. The laser input and prism are shown schematically, and the image indicates propagation. (b) Wafer characterization, indicating a thickness of $817 \pm 1 \text{ nm}$ at nine points and the tensile-stress map with a mean of $38 \pm 7 \text{ MPa}$; (c) SEM image of a 46 μm diameter ring resonator. Inset shows the ring waveguide; (d) fabrication process flow, including IBS deposition, electron-beam lithography, tantala etching, UV lithography, Si etching, and thermal annealing; (e) resonator line shape (black trace) with FWHM of 100 MHz, calibrated by a 200 MHz free-spectral range fiber Mach-Zehnder interferometer (red trace); (f) characterization of n_2 by P_{th} for parametric oscillation versus coupling Q_L . The blue and red lines indicate the expected change in P_{th} in the undercoupled regime. (g) Temperature dependence of ring resonator frequency.

transfers roughness to waveguide structures; this effect should be addressed to reduce waveguide losses. We optionally create a silica upper cladding, using inductively coupled plasma chemical vapor deposition (ICP CVD). Future work would utilize plasma-enhanced CVD silica claddings [33]. To satisfy four-wave-mixing phase matching at 1550 nm, 800 nm (570 nm) tantala films are appropriate in the case of silica (air) cladding on the top and sides of waveguides. We fabricate numerous nonlinear photonics designs that are organized into chips, which we dice from the full wafer using UV laser lithography and an Si deep reactive ion etch. Thermal annealing of the tantala film in a nitrogen and oxygen background gas is critical.

We explore the efficiency of Kerr nonlinear processes with our fabricated tantala devices. In particular for ring resonators [Fig. 1(c)], we measure Q , the nonlinear refractive index (n_2), and the thermo-optic coefficient (dn/dT), which are key determinants for Kerr soliton microcombs. To understand how large a quality factor (Q) we can achieve in tantala, we fabricate ring resonators with an RW of 5 μm to reduce the effects of scattering from the etched sidewall of the waveguide [34]. We test with a <100 kHz linewidth, 1550 nm laser, which is calibrated by a fiber Mach–Zehnder interferometer; see Fig. 1(e). We determine the loaded $Q_L = 1.9 \times 10^6$, which enables us to estimate the internal $Q_{\text{int}} \approx 3.8 \times 10^6$ based on the transmitted power that is roughly consistent with critical coupling. The corresponding propagation loss is 8 dB/m. To understand the nonlinear refractive index (n_2) of tantala, we measure the required on-chip threshold power (P_{th}) to observe parametric oscillation in devices of 570 nm thickness with air cladding on top and sides. Measurements with 15 separate ring resonators in which Q_L is varied over a small range are shown in Fig. 1(f). Based on knowledge of the ring-resonator mode volume, Q_L , and refractive index, we estimate nonlinear refractive index $n_2 = 6.2 \pm 2.3 \times 10^{-19} \text{ m}^2/\text{W}$ from calculation of the threshold power [35]. Our n_2 measurement is consistent with a previous precision determination [30], and it is a factor of 2 smaller than a measurement with material annealed at higher temperature [32].

Oxygen vacancy and crystallization attributes in tantala are fascinating effects that influence losses and nonlinearity. To understand the thermo-optic coefficient [Fig. 1(g)] of our tantala ring resonators, we monitor the thermo-optic shift in resonance frequency of a particular mode as we heat the temperature of the entire chip. From the slope, we determine $dn/dT \approx -\frac{n}{v} \frac{dv}{dT} \approx 8.8 \times 10^{-6} \text{ K}^{-1}$, where n is the refractive index and v is optical frequency.

3. QUALITY FACTOR MEASUREMENTS IN TANTALA RING RESONATORS

Since high Q_{int} is critical for numerous applications of integrated photonics resonators, in Fig. 2 we explore how the processing and design of tantala devices influence loss. All of the devices considered in Fig. 2 are fabricated with ring resonators of 46 μm diameter, 570 nm tantala thickness, and without a top oxide cladding. As part of our fabrication process flow [Fig. 1(d)], we anneal the tantala material at relatively high temperature. Figure 2(a) shows the dependence of Q_{int} as we vary the maximum annealing temperature from 480 C to 900 C; we find little benefit in annealing longer than 5 h. We observe an improvement in Q_{int} until 600 C, especially in the presence of an oxygen background gas that may reduce microdefects in oxygen-poor IBS tantala films [26,36]. Beyond 600 C, we presume the tantala film forms a polycrystalline state [inset of Fig. 2(a)] that does not readily offer low loss [37]; however, future investigations should consider optimized deposition or postprocessing to utilize single-crystal states [37].

A second challenge in obtaining high Q_{int} is material scattering and absorption losses, particularly across the broad visible to infrared bands needed for contemporary applications. To characterize scattering loss, we vary RW in fabricated devices from 1 to 5 μm and measure Q_{int} ; see Fig. 2(b). The intrinsic quality factor improves by increasing RW to 3 μm , beyond which our simulations indicate that the mode profile is largely protected from the etched sidewall surface. Simulated TE mode profiles (insets) show that the mode intensity at the waveguide sidewall

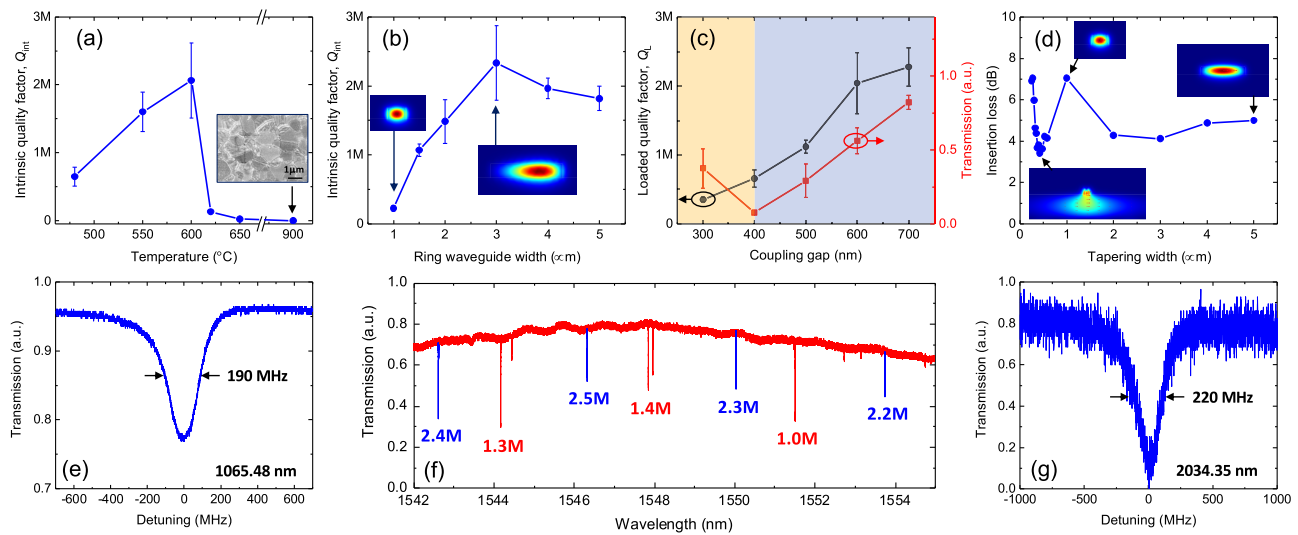


Fig. 2. Quality-factor measurements of tantala resonators, fabricated with a 570 nm film. (a) Q_{int} versus annealing temperature of a 3 μm RW resonator. Inset, SEM image of a presumably crystallized tantala film, following annealing to 900 C; (b) Q_{int} versus RW. Annealing to 600 C for 6 h. Inset, mode profiles with 1 and 3 μm RW; (c) Q_L and normalized transmission versus coupling gap for a 3 μm RW; (d) edge-coupling insertion loss with a lensed fiber versus inverse taper width; inset, simulated mode profiles for narrow, intermediate, and wide inverse tapers; (e) resonator line shape, indicating $Q_{\text{int}} = 1.6 \times 10^6$; (f) normalized resonator transmission versus wavelength in the C-band. Labels indicate Q_L for the TE00 (blue) and TE01 (red) modes with a 600 nm coupling gap; (g) resonator line shape, indicating $Q_{\text{int}} = 1 \times 10^6$.

with $RW = 3 \mu\text{m}$ is less than $RW = 1 \mu\text{m}$. Moreover, for RW less than $3 \mu\text{m}$, we observe resonance-mode splitting characteristic of scattering. We control the resonator coupling rate and chip-edge coupling through e-beam lithography. Figure 2(c) demonstrates a Q_L tuning across the critical-coupling regime. Figure 2(d) shows that relatively low-loss edge coupling to lensed fibers with a $2.5 \mu\text{m}$ mode-field diameter is also possible, using inverse tapers in which the waveguide width (WW) is reduced at the chip edge. Even in devices with air cladding on the top and sides, $>2 \mu\text{m}$ wide waveguides tapered at the chip edge provide ≈ -4 dB per facet due to the large mode size of the wide waveguide. Intermediate-width inverse tapers ≈ 500 -nm wide edge provide ≈ -3 dB per facet by expanding the mode into the silica cladding. Here, we utilize an inverse taper length of $20 \mu\text{m}$, which causes negligible loss.

Figures 2(e)–2(g) explore Q_{int} measurements across the near-infrared wavelength bands of 1–2 μm . We utilize $3 \mu\text{m}$ RW devices optimized for 1550 nm operation, and we measure Q_L with tunable lasers at 1065 nm [Fig. 2(e)], the 1550 nm band [Fig. 2(f)], and 2034 nm [Fig. 2(g)]. Apparently, tantala ring resonators offer high $Q_{\text{int}} > 10^6$ over at least this wavelength range, consistent with the material's reported wide transparency [27]. In particular, across the 1550 nm range, we do not observe wavelength-dependent deterioration of Q_{int} , and we also observe high Q_{int} in the 1300 nm wavelength band. Our Q_{int} measurements do not appear to be constrained by tantala absorption; indeed, tantala's use in low-loss, bulk reflectors indicates the possibility for Q_{int} at least 2 times higher than our present results [38].

4. KERR SOLITON FREQUENCY-COMB GENERATION

As an application of our high- Q tantala ring resonator platform, we explore Kerr soliton frequency-comb generation; see Fig. 3. Using a tantala device layer thickness of 570 nm, we fabricate ring resonators with a $46\text{-}\mu\text{m}$ radius and two settings of RW, i.e., 1.6 and $1.65 \mu\text{m}$, which support ultrabroad bandwidth anomalous group velocity dispersion (GVD) and anomalous-to-normal GVD transitions for dispersive-wave engineering [5]. We use a

coupling gap of 500 or 600 nm between the ring and a straight waveguide to achieve a slight undercoupling in the 1550 nm band.

We stabilize single soliton pulses in these devices by use of the fast pump-laser-frequency ramping technique [5,35]. Figures 3(a) and 3(c) show the outcoupled spectrum of the soliton in the two RW geometries, including losses from off-chip coupling to lensed fiber. Reduced thermo-optic frequency shifts in our tantala resonators facilitate qualitatively easier soliton capture and a reduced requirement for the laser-frequency scan range compared to our experience with SiN resonators. In Figs. 3(b) and 3(d), we show a different perspective of the soliton spectra, namely, their linear power spectra and comparison to $\text{sech}^2(\nu)$ fit. We estimate a full width at half-maximum (FWHM) of 9.8 THz (12.6 THz) for the device with RW of $1.6 \mu\text{m}$ ($1.65 \mu\text{m}$), corresponding to an estimated soliton pulse duration inside the resonator of 32 fs (25 fs), respectively. To understand the wavelengths of dispersive-wave generation in our devices, we consider the integrated dispersion $D_{\text{int}} \equiv \omega_{\mu} - (\omega_0 + D_1\mu)$, which we obtain from refractive-index data [39] and finite-element simulations of the resonator modes. For these RW values, we anticipate the dispersive-wave peaks to appear in the range of 2100 nm, which is consistent with our observations. Unfortunately, the wavelength-dependent coupling rate from the ring resonator to a straight on-chip waveguide, providing a single point of smallest gap between the resonator and coupler, substantially reduces the soliton intensity below ~ 1400 nm, obscuring the dispersive-wave generation expected around 1100 nm in this device. Pulley couplers with an extended interaction length between the ring and waveguide have been shown to alleviate this issue, and we plan to utilize such designs in future devices [5]. Increasing knowledge of refractive indices will impact future device designs [40]. From the 20 mW threshold power for frequency-comb generation, we obtain another estimate of the nonlinear refractive index (n_2) of our tantala material that is consistent with our results in Fig. 1(f).

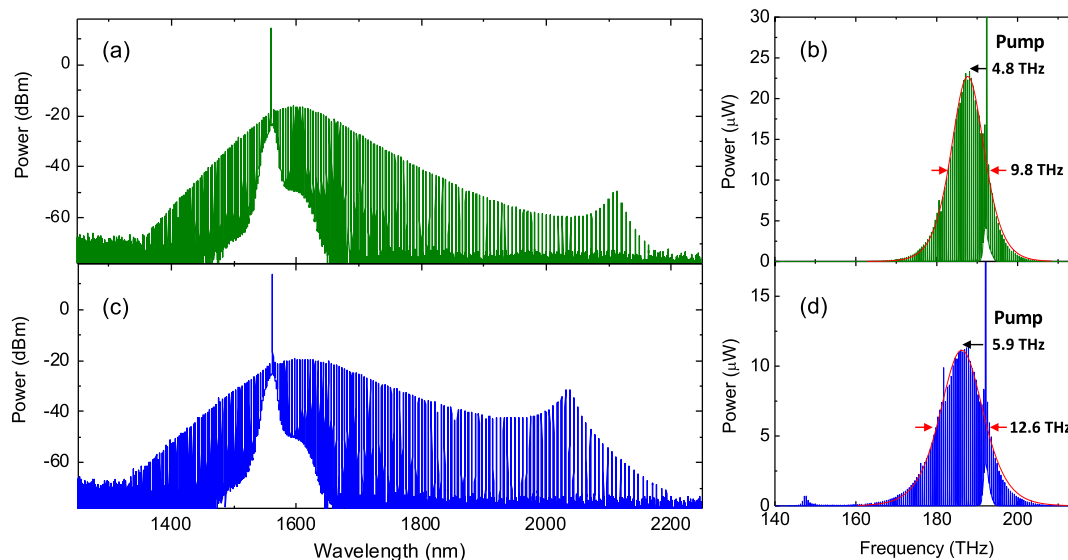


Fig. 3. Soliton generation in tantala ring resonators. (a) Observed single-soliton frequency-comb spectrum with a $1.6 \mu\text{m}$ RW. Dispersive-wave power enhancements of the spectrum are observed into the 2000 nm wavelength range. (b) Linear scale plot of the spectrum in (a), highlighting the FWHM bandwidth; (c) idem of (a) but with a $1.65 \mu\text{m}$ RW; (d) linear-scale plot of the spectrum in (c).

5. SUPERCONTINUUM GENERATION IN TANTALA WAVEGUIDES

As a second characterization technique of our low-loss tantala integrated photonics platform, we explore waveguide supercontinuum generation from input mode-locked laser pulses [30,41,42]. The large n_2 index and wide transparency window has the potential to support a variety of supercontinuum device concepts, including low-power frequency combs for optical metrology [43], few-cycle pulse generation [7], and mid-infrared photonics waveguides either via suspended structures [44] or with tantala as a cladding material. These experiments utilize our 820 and 570 nm thick tantala films, and an erbium fiber mode-locked laser provides pulses with 80 fs duration, a repetition frequency of 100 MHz, and 0.5 nJ maximum pulse energy [7].

Figures 4(a) and 4(b) explore how GVD engineering by changing the WW controls the supercontinuum spectrum. In particular, we use an 820 nm thick tantala device layer composed of a waveguide, and we apply top and side claddings with ICP CVD SiO₂. To bring laser pulses on and off chip, we increase (decrease) the WW over a 0.02 mm length at the chip edges in air-clad (oxide-clad) chips to expand the optical mode in the plane of the chip with minimal wavelength dependence. Therefore, we accomplish input coupling with an aspheric lens and output coupling with lensed fiber at an efficiency of 40%–50% at each facet, depending on the coupling technique and cladding material. We couple to the fundamental spatial mode of the waveguide, consistent with our WW design to achieve a supercontinuum spanning the second

harmonic of the pump. The tantala waveguide section for supercontinuum is 5 mm in length, and we vary the GVD in this section by the WW through fabrication of ~ 20 devices on one chip. We measure the supercontinuum spectrum [Fig. 4(a)] by coupling the waveguide output to optical spectrum analyzers that cover 350–5700 nm with an IR-compatible multimode fiber. Our results indicate that we can create supercontinuum light in the range of 500–2500 nm, with a wide potential for design based on single or multiple WW sections [45]. This closely agrees with our expectation [Fig. 4(b)], based on finite-element method GVD simulations input to nonlinear Schrödinger equation simulations. The abrupt loss of observed supercontinuum intensity at wavelengths longer than 2500 nm is consistent with O-H absorption in the SiO₂ cladding, highlighting the opportunity to develop suspended or ridge-waveguide structures without a second material cladding.

Low-power operation is a key for many supercontinuum applications; therefore, we explore supercontinuum generation in 570 nm thick waveguides without SiO₂ cladding that offer the lowest optical loss within our existing nanofabrication process. Our results here indicate the low waveguide-coupled pulse energy necessary for supercontinuum, forming the basis for future experiments with tantala. With air cladding on the top and side, this waveguide thickness is in the optimum range for ultrabroad supercontinuum, particularly f-2f self-referencing with dispersive-wave emission at the second-harmonic wavelength of the input laser. We present a systematic characterization of supercontinuum generation versus on-chip input pulse energy for an air-clad waveguide of WW = 1.5 μm , with Figs. 4(c) and 4(d) showing the spectrum spanning 750 to 2400 nm with a 100 pJ input and the spectrum versus pulse energy from 0 to 150 pJ, respectively. Here, the minimum pulse energy to energize the ~ 780 nm dispersive wave is 60 pJ, which is comparable to the power needed for supercontinuum in the more mature SiN platform [43]. We estimate chip coupling losses at low pulse energy with identical lensed fibers at the input and output facets, assuming negligible loss in the 5 mm long waveguide section. By measuring several devices on one chip, we assess average performance. With an understanding of the loss per facet to lensed fiber, we can account for modestly improved input coupling when we use an aspheric lens at the input. Then, according to an optical power measurement immediately prior to the aspheric lens, we estimate the on-chip power. Optimization of scattering and absorption losses in tantala waveguides are a key goal for reduced pulse-energy requirements [46].

6. CONCLUSION

In summary, we have reported an integrated nonlinear photonics platform based on tantala, which offers ultrabroad bandwidth Kerr microresonator solitons and waveguide supercontinuum generation. The key advantages of tantala are: essentially zero tensile stress even in very thick >800 nm films and <1 nm flatness; a low optical loss <8 dB/m; and a high nonlinear coefficient thrice that of SiN. With these features, we realize a high yield of tantala devices designed to leverage nonlinear optics, without mitigation strategies for film cracking. In the future, we anticipate leveraging tantala's wide transparency window from 320 to 8000 nm for visible and mid-infrared integrated photonics, which we can access either with SiO₂ claddings or without a cladding by way of thick tantala ridge-waveguide structures or suspended tantala waveguides, respectively. Moreover, the low thermo-optic coefficient

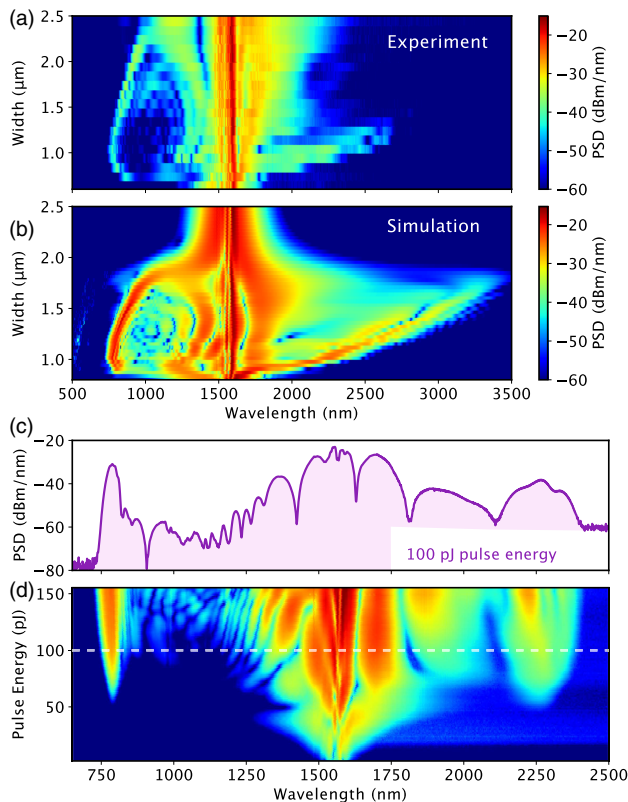


Fig. 4. Supercontinuum generation in tantala waveguides. (a) Experimental and (b) simulated output spectra versus WW for 820-nm-thick waveguides with a full SiO₂ cladding. We attribute attenuation at wavelengths beyond 2700 nm to absorption in the SiO₂ cladding. (c), (d) Input power dependence of supercontinuum for a 570-nm-thick, WW = 1.5 μm tantala waveguide without SiO₂ upper cladding. The trace in (c) corresponds to the white, horizontal line at 100 pJ in (d).

of tantala would offer Kerr solitons with reduced fundamental thermo-refractive noise [47].

Funding. National Institute of Standards and Technology (NIST-on-a-Chip); Defense Advanced Research Projects Agency (ACES); Defense Advanced Research Projects Agency (DODOS).

Acknowledgment. The authors thank Jennifer Black, Jizhao Zang, and Kartik Srinivasan for helpful comments, and Jeff Chiles and the Boulder Microfabrication Facility. Trade names are provided to disseminate information and do not constitute an endorsement. This work is not subject to copyright in the U.S.

Disclosures. David Carlson is a Founder of Octave Photonics. The remaining authors declare no conflicts of interest.

Data Availability. Data underlying the results presented in this paper are not publicly available at this time but may be obtained from the authors upon reasonable request.

REFERENCES

1. X. Lu, G. Moille, Q. Li, D. A. Westly, A. Singh, A. Rao, S.-P. Yu, T. C. Briles, S. B. Papp, and K. Srinivasan, "Efficient telecom-to-visible spectral translation through ultralow power nonlinear nanophotonics," *Nat. Photonics* **13**, 593–601 (2019).
2. K. Tai, A. Hasegawa, and A. Tomita, "Observation of modulational instability in optical fibers," *Phys. Rev. Lett.* **56**, 135–138 (1986).
3. S. Barland, J. R. Tredicce, M. Brambilla, L. A. Lugiato, S. Balle, M. Giudici, T. Maggipinto, L. Spinelli, G. Tissoni, T. Knödl, M. Miller, and R. Jäger, "Cavity solitons as pixels in semiconductor microcavities," *Nature* **419**, 699–702 (2002).
4. T. J. Kippenberg, A. L. Gaeta, M. Lipson, and M. L. Gorodetsky, "Dissipative Kerr solitons in optical microresonators," *Science* **361**, eaan8083 (2018).
5. T. C. Briles, J. R. Stone, T. E. Drake, D. T. Spencer, C. Fredrick, Q. Li, D. Westly, B. R. Ilic, K. Srinivasan, S. A. Diddams, and S. B. Papp, "Interlocking Kerr-microresonator frequency combs for microwave to optical synthesis," *Opt. Lett.* **43**, 2933–2936 (2018).
6. T. E. Drake, T. C. Briles, J. R. Stone, D. T. Spencer, D. R. Carlson, D. D. Hickstein, Q. Li, D. Westly, K. Srinivasan, S. A. Diddams, and S. B. Papp, "Terahertz-rate Kerr-microresonator optical clockwork," *Phys. Rev. X* **9**, 031023 (2019).
7. D. R. Carlson, P. Hutchison, P. Hutchison, D. D. Hickstein, S. B. Papp, and S. B. Papp, "Generating few-cycle pulses with integrated nonlinear photonics," *Opt. Express* **27**, 37374–37382 (2019).
8. D. Marpaung, J. Yao, and J. Capmany, "Integrated microwave photonics," *Nat. Photonics* **13**, 80–90 (2019).
9. D. J. Blumenthal, H. Ballani, R. O. Behunin, J. E. Bowers, P. Costa, D. Lenoski, P. A. Morton, S. Papp, and P. T. Rakich, "Frequency stabilized links for coherent WDM fiber interconnects in the datacenter," *J. Lightwave Technol.* **38**, 3376–3386 (2020).
10. M. A. Tran, D. Huang, and J. E. Bowers, "Tutorial on narrow linewidth tunable semiconductor lasers using Si/III-V heterogeneous integration," *APL Photon.* **4**, 111101 (2019).
11. J. Liu, A. S. Raja, M. Karpov, B. Ghadiani, M. H. P. Pfeiffer, B. Du, N. J. Engels, H. Guo, M. Zervas, and T. J. Kippenberg, "Ultralow-power chip-based soliton microcombs for photonic integration," *Optica* **5**, 1347–1353 (2018).
12. D. J. Moss, R. Morandotti, A. L. Gaeta, and M. Lipson, "New CMOS-compatible platforms based on silicon nitride and Hydex for nonlinear optics," *Nat. Photonics* **7**, 597–607 (2013).
13. J. S. Levy, A. Gondarenko, M. A. Foster, A. C. Turner-Foster, A. L. Gaeta, and M. Lipson, "CMOS-compatible multiple-wavelength oscillator for on-chip optical interconnects," *Nat. Photonics* **4**, 37–40 (2010).
14. M. H. P. Pfeiffer, A. Kordts, V. Brasch, M. Zervas, M. Geiselmann, J. D. Jost, and T. J. Kippenberg, "Photonic Damascene process for integrated high-Q microresonator based nonlinear photonics," *Optica* **3**, 20–25 (2016).
15. K. Y. Yang, D. Y. Oh, S. H. Lee, Q.-F. Yang, X. Yi, B. Shen, H. Wang, and K. Vahala, "Bridging ultrahigh-Q devices and photonic circuits," *Nat. Photonics* **12**, 297–302 (2018).
16. J. Chiles, N. Nader, D. D. Hickstein, S. P. Yu, T. C. Briles, D. Carlson, H. Jung, J. M. Shainline, S. Diddams, S. B. Papp, S. W. Nam, and R. P. Mirin, "Deuterated silicon nitride photonic devices for broadband optical frequency comb generation," *Opt. Lett.* **43**, 1527–1530 (2018).
17. X. Xu, M. Tan, J. Wu, T. G. Nguyen, S. T. Chu, B. E. Little, R. Morandotti, A. Mitchell, and D. J. Moss, "High performance RF filters via bandwidth scaling with Kerr micro-combs," *APL Photon.* **4**, 026102 (2019).
18. Z. Gong, A. Bruch, M. Shen, X. Guo, H. Jung, L. Fan, X. Liu, L. Zhang, J. Wang, J. Li, J. Yan, and H. X. Tang, "High-fidelity cavity soliton generation in crystalline AlN micro-ring resonators," *Opt. Lett.* **43**, 4366–4369 (2018).
19. L. Chang, W. Xie, H. Shu, Q. Yang, B. Shen, A. Boes, J. D. Peters, W. Jin, S. Liu, G. Moille, S.-P. Yu, X. Wang, K. Srinivasan, S. B. Papp, K. Vahala, and J. E. Bowers, "Ultra-efficient frequency comb generation in AlGaAs-on-insulator microresonators," arXiv:1909.09778 [physics] (2019).
20. Z. Gong, X. Liu, Y. Xu, M. Xu, J. B. Surya, J. Lu, A. Bruch, C. Zou, and H. X. Tang, "Soliton microcomb generation at 2 μm in z-cut lithium niobate microring resonators," *Opt. Lett.* **44**, 3182–3185 (2019).
21. D. J. Wilson, K. Schneider, S. Hönl, M. Anderson, Y. Baumgartner, L. Czornomaz, T. J. Kippenberg, and P. Seidler, "Integrated gallium phosphide nonlinear photonics," *Nat. Photonics* **14**, 57–62 (2020).
22. M.-J. Lee, C. B. Lee, D. Lee, S. R. Lee, M. Chang, J. H. Hur, Y.-B. Kim, C.-J. Kim, D. H. Seo, S. Seo, U.-I. Chung, I.-K. Yoo, and K. Kim, "A fast, high-endurance and scalable non-volatile memory device made from asymmetric Ta_2O_5 -x/ TaO_2 -x bilayer structures," *Nat. Mater.* **10**, 625–630 (2011).
23. G. Rempe, R. J. Thompson, H. J. Kimble, and R. Lalezari, "Measurement of ultralow losses in an optical interferometer," *Opt. Lett.* **17**, 363–365 (1992).
24. C.-L. Wu, C.-H. Hsieh, G.-R. Lin, W.-C. Chi, Y.-J. Chiu, Y.-Y. Lin, Y.-J. Hung, M.-H. Shih, A.-K. Chu, and C.-K. Lee, "Tens of GHz Tantalum pentoxide-based micro-ring all-optical modulator for Si photonics," *Ann. Phys. (Leipzig)* **529**, 1600358 (2017).
25. C.-L. Wu, J.-Y. Huang, D.-H. Ou, T.-W. Liao, Y.-J. Chiu, M.-H. Shih, Y.-Y. Lin, A.-K. Chu, and C.-K. Lee, "Efficient wavelength conversion with low operation power in a Ta_2O_5 -based micro-ring resonator," *Opt. Lett.* **42**, 4804–4807 (2017).
26. H. Demiryont, J. R. Sites, and K. Geib, "Effects of oxygen content on the optical properties of tantalum oxide films deposited by ion-beam sputtering," *Appl. Opt.* **24**, 490–495 (1985).
27. M. Belt, M. L. Davenport, J. E. Bowers, and D. J. Blumenthal, "Ultra-low-loss Ta_2O_5 -core/ SiO_2 -clad planar waveguides on Si substrates," *Optica* **4**, 532–536 (2017).
28. M. R. Abernathy, X. Liu, T. H. Metcalf, M. R. Abernathy, X. Liu, and T. H. Metcalf, "An overview of research into low internal friction optical coatings by the gravitational wave detection community," *Mater. Res.* **21**, e20170863 (2018).
29. M. S. Farhan, E. Zalnezhad, and A. R. Bushroa, "Properties of Ta_2O_5 thin films prepared by ion-assisted deposition," *Mater. Res. Bull.* **48**(10), 4206–4209 (2013).
30. C.-Y. Tai, J. S. Wilkinson, N. M. B. Perney, M. C. Netti, F. Cattaneo, C. E. Finlayson, and J. J. Baumberg, "Determination of nonlinear refractive index in a Ta_2O_5 rib waveguide using self-phase modulation," *Opt. Express* **12**, 5110–5116 (2004).
31. C.-L. Wu, Y.-J. Chiu, C.-L. Chen, Y.-Y. Lin, A.-K. Chu, and C.-K. Lee, "Four-wave-mixing in the loss low submicrometer Ta_2O_5 channel waveguide," *Opt. Lett.* **40**, 4528–4531 (2015).
32. C.-L. Wu, B.-T. Chen, Y.-Y. Lin, W.-C. Tien, G.-R. Lin, Y.-J. Chiu, Y.-J. Hung, A.-K. Chu, and C.-K. Lee, "Low-loss and high-Q Ta_2O_5 based micro-ring resonator with inverse taper structure," *Opt. Express* **23**, 26268–26275 (2015).
33. W. Jin, D. D. John, J. F. Bauters, T. Bosch, B. J. Thibeault, and J. E. Bowers, "Deuterated silicon dioxide for heterogeneous integration of ultra-low-loss waveguides," *Opt. Lett.* **45**, 3340–3343 (2020).
34. X. Ji, F. A. S. Barbosa, S. P. Roberts, A. Dutt, J. Cardenas, Y. Okawachi, A. Bryant, A. L. Gaeta, and M. Lipson, "Ultra-low-loss on-chip resonators with sub-milliwatt parametric oscillation threshold," *Optica* **4**, 619–624 (2017).
35. T. C. Briles, S.-P. Yu, T. E. Drake, J. R. Stone, and S. B. Papp, "Generating octave-bandwidth soliton frequency combs with compact, low-power semiconductor lasers," *Phys. Rev. Appl.* **14**, 014006 (2020).
36. R. Ramprasad, "First principles study of oxygen vacancy defects in tantalum pentoxide," *J. Appl. Phys.* **94**, 5609–5612 (2003).

37. Y. Yang and Y. Kawazoe, "Prediction of new ground-state crystal structure of Ta_2O_5 ," *Phys. Rev. Mater.* **2**, 034602 (2018).
38. L. Pinard, B. Sassolas, R. Flaminio, D. Forest, A. Lacoudre, C. Michel, J. L. Montorio, and N. Morgado, "Toward a new generation of low-loss mirrors for the advanced gravitational waves interferometers," *Opt. Lett.* **36**, 1407–1409 (2011).
39. L. Gao, F. Lemarchand, and M. Lequime, "Exploitation of multiple incidences spectrometric measurements for thin film reverse engineering," *Opt. Express* **20**, 15734–15751 (2012).
40. J. A. Black, R. Streater, K. F. Lamee, D. R. Carlson, S.-P. Yu, and S. B. Papp, "Group-velocity dispersion engineering of tantala integrated photonics," *Opt. Lett.* **46**, 817–820 (2020).
41. R. Fan, C.-L. Wu, Y.-Y. Lin, C.-Y. Liu, P.-S. Hwang, C.-W. Liu, J. Qiao, M.-H. Shih, Y.-J. Hung, Y.-J. Chiu, A.-K. Chu, and C.-K. Lee, "Visible to near-infrared octave spanning supercontinuum generation in tantalum pentoxide (Ta_2O_5) air-cladding waveguide," *Opt. Lett.* **44**, 1512–1515 (2019).
42. J. R. C. Woods, J. Daykin, A. S. K. Tong, C. Lacava, P. Petropoulos, A. C. Tropper, P. Horak, J. S. Wilkinson, and V. Apostolopoulos, "Supercontinuum generation in tantalum pentoxide waveguides for pump wavelengths in the 900 nm to 1500 nm spectral region," *Opt. Express* **28**, 32173–32184 (2020).
43. D. R. Carlson, D. D. Hickstein, A. Lind, J. B. Olson, R. W. Fox, R. C. Brown, A. D. Ludlow, Q. Li, D. Westly, H. Leopardi, T. M. Fortier, K. Srinivasan, S. A. Diddams, and S. B. Papp, "Photonic-chip supercontinuum with tailored spectra for counting optical frequencies," *Phys. Rev. Appl.* **8**, 014027 (2017).
44. Z. Cheng, X. Chen, C. Y. Wong, K. Xu, and H. K. Tsang, "Mid-infrared suspended membrane waveguide and ring resonator on silicon-on-insulator," *IEEE Photon. J.* **4**, 1510–1519 (2012).
45. D. D. Hickstein, H. Jung, D. R. Carlson, A. Lind, I. Coddington, K. Srinivasan, G. G. Ycas, D. C. Cole, A. Kowligy, C. Fredrick, S. Droste, E. S. Lamb, N. R. Newbury, H. X. Tang, S. A. Diddams, and S. B. Papp, "Ultrabroadband supercontinuum generation and frequency-comb stabilization using on-chip waveguides with both cubic and quadratic nonlinearities," *Phys. Rev. Appl.* **8**, 014025 (2017).
46. K. F. Lamee, D. R. Carlson, Z. L. Newman, S.-P. Yu, and S. B. Papp, "Nanophotonic tantala waveguides for supercontinuum generation pumped at 1560 nm," *Opt. Lett.* **45**, 4192–4195 (2020).
47. T. E. Drake, J. R. Stone, T. C. Briles, and S. B. Papp, "Thermal decoherence and laser cooling of Kerr microresonator solitons," *Nat. Photonics* **14**, 480–485 (2020).